

# High-Performance, Solution-Processed, Embedded Multiscale Metallic Transparent Conductors

Yong Suk Oh,<sup>†</sup> Hyunwoo Lee,<sup>‡</sup> Dong Yun Choi,<sup>†</sup> Sung-Uk Lee,<sup>†</sup> Hojin Kim,<sup>§</sup> Seunghyup Yoo,<sup>‡</sup> Inkyu Park,<sup>†</sup> and Hyung Jin Sung<sup>\*,†</sup>

<sup>†</sup>Department of Mechanical Engineering, KAIST, 291 Daehak-ro, Yuseong-gu, Daejeon 34141, Korea

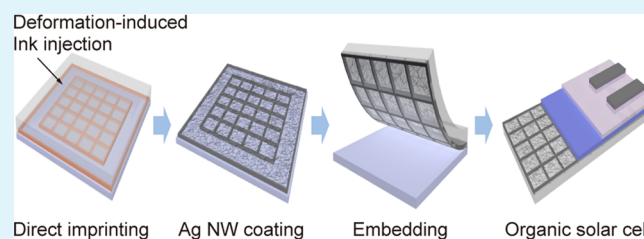
<sup>‡</sup>Department of Electrical Engineering, KAIST, 291 Daehak-ro, Yuseong-gu, Daejeon 34141, Korea

<sup>§</sup>Department of Mechanical Engineering, POSTECH, 77 Cheongam-ro, Pohang, Kyungbuk 37673, Korea

## S Supporting Information

**ABSTRACT:** High-performance multiscale metallic transparent conductors (TCs) are demonstrated by incorporating Ag nanowire (NW) networks into microscale Ag grid structures. Highly conductive Ag grids are fabricated via direct imprinting of an Ag ion ink using a reservoir-assisted mold. In this mold, a macroscale cavity, called the “reservoir”, is designed to connect to a grid-patterned cavity. The reservoir has a large cavity volume, which reduces unwanted residual layers within the grid spacings by introducing a thinner liquid film. The reservoir undergoes a large volume reduction during mold deformation, which improves ink filling within the grid-patterned cavity through deformation-induced ink injection. The multiscale metallic TCs show a sheet resistance ( $R_s$ ) of  $<1.5 \Omega/\text{sq}$  and a transmittance ( $T$ ) of 86% at 550 nm, superior to the corresponding values of Ag NW networks ( $R_s$  of  $15.6 \Omega/\text{sq}$  at a similar  $T$ ). We estimate the  $R_s$ – $T$  performances of the Ag grids using geometrical calculations and demonstrate that their integration can enhance the opto-electrical properties of the Ag NW networks. Multiscale metallic TCs are successfully transferred and embedded into a transparent, flexible, and UV-curable polymer matrix. The embedded multiscale metallic TCs show reasonable electromechanical and chemical stability. The utility of these TCs is demonstrated by fabricating flexible organic solar cells.

**KEYWORDS:** direct imprinting, metal grid, silver nanowire, embedding, transparent conductor



## 1. INTRODUCTION

Transparent conductors (TCs) are critical to the operation of various transparent optoelectronic devices, including photovoltaic cells,<sup>1</sup> organic light-emitting diodes,<sup>2</sup> and touch screen panels.<sup>3</sup> Indium tin oxide (ITO) is the most widely used transparent conductive material due to its low sheet resistance ( $R_s$ ) and excellent optical transmittance ( $T$ ); however, the inherent brittleness of ITO renders it unsuitable for flexible optoelectronic applications,<sup>4</sup> and alternatives to ITO, such as conducting polymers,<sup>5</sup> graphene,<sup>6,7</sup> carbon nanotubes,<sup>8,9</sup> metal nanowire (NW) networks,<sup>10,11</sup> and regular metal grids,<sup>12,13</sup> have been actively developed. In particular, metallic TCs, including NW networks and micro/nanoscale metal grids, provide superior electrical and optical properties as compared to other materials. Among the metallic TCs developed thus far, Ag NW networks are advantageous due to their low manufacturing cost, good mechanical flexibility, and excellent opto-electrical properties.<sup>10,14</sup> Despite these advantages, the opto-electrical properties of Ag NW networks are not yet comparable to those of ITO ( $R_s = 10 \Omega/\text{sq}$  and  $T = 90\%$ ), a requirement for next-generation optoelectronic applications.<sup>11,15</sup>

Several research groups have systematically investigated the  $R_s$ – $T$  performances of Ag NW networks as a function of the NW diameter and length, areal coverage, and junction resistance between the NWs. Bergin et al.<sup>16</sup> reported an experimental study of the opto-electrical properties of Ag NW networks as a function of the diameter and length of the NWs and the areal coverage. Their experimental results agreed with the theoretical predictions for 2D widthless stick systems. De et al.<sup>17</sup> suggested that a percolative figure of merit (FoM) could explain the relationship between  $R_s$  and  $T$  of Ag NW networks for high transmittance of  $T > 90\%$ . Networks of small-diameter Ag NWs yielded a higher percolative FoM than those of large-diameter Ag NWs, and Ag NWs with diameters below 20 nm are required to achieve  $R_s = 10 \Omega/\text{sq}$  at  $T = 90\%$ . Mutiso et al.<sup>11</sup> theoretically demonstrated that Ag NWs longer than  $32 \mu\text{m}$  are needed to achieve  $R_s \leq 10 \Omega/\text{sq}$  at  $T = 90\%$  for fixed diameter of 40 nm and junction resistance of 2 k $\Omega$ . Lee et al.<sup>18,19</sup> experimentally demonstrated that networks of very long Ag NWs ( $500 \mu\text{m}$ ) prepared via a successive multistep synthesis

Received: February 25, 2016

Accepted: April 13, 2016

Published: April 13, 2016

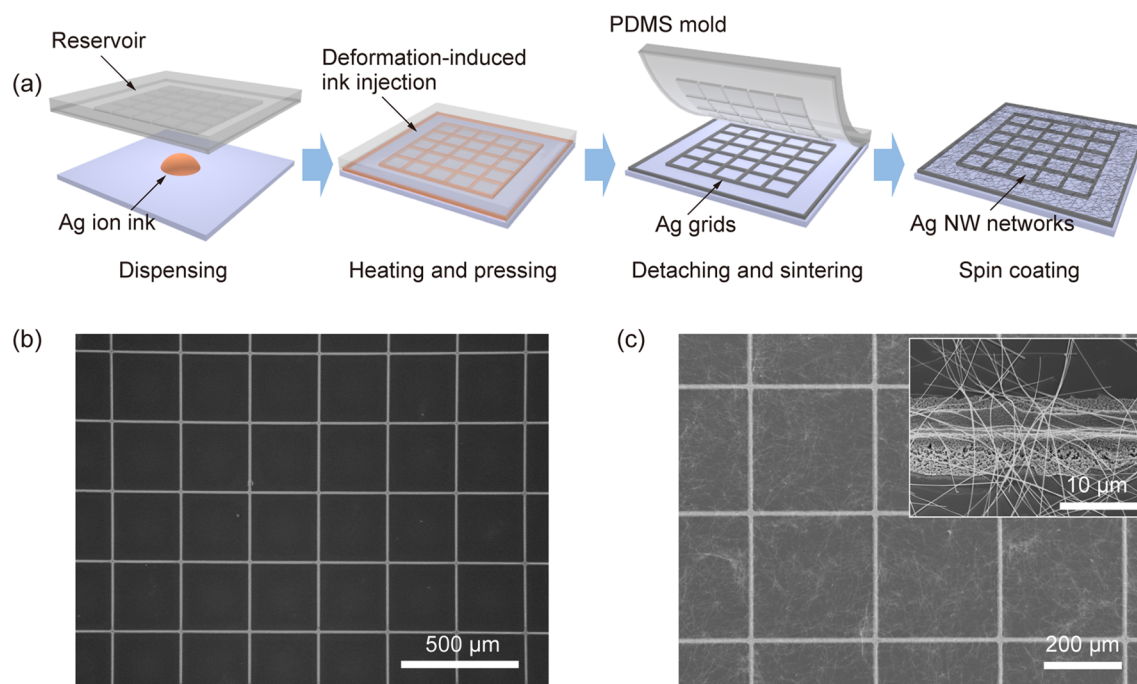


**Figure 1.** (a) Fabrication of the multiscale metallic TCs based on the Ag grid-NWs. (b) SEM image of the Ag grid structure-patterned on the glass substrate. (c) SEM image of the Ag NW coating on the Ag grid structures. The inset shows a magnified SEM image of the Ag NWs randomly overlapping with the Ag grid structures.

performed better ( $R_s = 9 \Omega/\text{sq}$  and  $T_{550 \text{ nm}} = 89\%$ ) than currently available Ag NW networks. The multistep synthesis procedure required for the growth of very long NWs, however, suffered from complex and time-consuming processes. Ag NW networks prepared in conjunction with metal oxides<sup>20</sup> or graphene<sup>21</sup> were found to display lower junction resistances; however, the Ag NW-metal oxide TCs showed a limited flexibility and the Ag NW-graphene TCs exhibited a relatively higher sheet resistance ( $R_s = 22 \Omega/\text{sq}$  at  $T_{550 \text{ nm}} = 88\%$ ). Hsu et al.<sup>14</sup> demonstrated that hybrid TCs fabricated by incorporating microscale Cu wires and Ag NWs performed better than the Ag NW networks. Microscale Cu wires were able to transport electrons across long distances (10 mm) with much a higher conductance than the Ag NWs. This hybrid TCs showed an extremely low  $R_s = 0.36 \Omega/\text{sq}$  at  $T_{550 \text{ nm}} = 92\%$ . Microscale Cu wires were fabricated using thermal evaporation on electrospun polymer networks, which is not a simple or cost-effective process. Choi et al. suggested that solution-processed hybrid TCs could be prepared by incorporating Ag NWs into periodic microscale Ag nanoparticle (NP) wire array via convective self-assembly.<sup>22</sup> However, these Ag NP wires suffered from long processing time and asymmetric network structure, although performance improvement of the Ag NW networks ( $R_s = 5.7 \Omega/\text{sq}$  at  $T_{550 \text{ nm}} = 90\%$ ) could be achieved.

The incorporation of microscale regular metal grids into random Ag NW networks could achieve omnidirectional performance enhancement of Ag NW network. Metal grids offer many advantages: their grid widths and spacings are readily controlled, their conductance is bidirectional, and their junction resistance is low.<sup>23–30</sup> Solution-processed metal grids have been commonly fabricated using inkjet printing<sup>31</sup> and hot embossing techniques.<sup>12</sup> However, inkjet printing suffers from poor resolution ( $\sim 100 \mu\text{m}$ ), long processing time, and low throughput. Hot embossing process is required for two steps that are divided into thermal imprinting and ink filling.

Embedded metal grids are difficult to fabricate the hybrid Ag NW-metal grids TCs with low surface roughness.

Polydimethylsiloxane (PDMS)-based printing methods, including microcontact printing,<sup>32</sup> micromolding in capillaries,<sup>33</sup> and direct nanoimprinting,<sup>34,35</sup> can generate micro/nanoscale structures of functional nanomaterials, such as metal NPs, quantum dots and polymers at low cost and high-throughput.<sup>36–41</sup> Among these techniques, direct imprinting of colloidal metal NPs offers an effective technique for fabricating micro/nanoscale metal grid structures with negligible residual layers due to the low elasticity of PDMS mold, which provides conformal contact, the low surface energy of PDMS, which allows for easy detachment, and the high permeability of PDMS for degassing purposes.<sup>34,40,41</sup> Direct imprinting of colloidal metal NPs using a typical grid-patterned mold (T-mold) has not yet yielded high-performance metal grid TCs because concentrated colloidal NPs tend to be unstable, the ink filling tends to be insufficient, and unwanted residual layers tend to form. The fabrication of highly conductive metal grids over a large area ( $3 \times 3 \text{ cm}^2$ ) has been pursued by our group through the development of direct imprinting methods in which thermally reduced Ag NPs are imprinted using a reservoir-assisted mold (R-mold).<sup>42</sup> Highly conductive metal grids with a high surface roughness were transferred into a UV-curable polymer film using an embedding process. As a consequence, we could achieve low surface roughness of metallic TCs, which is a critical factor for the device compatibility in flexible optoelectronic applications.<sup>22,30,42–44</sup>

Here, we introduce the development of high-performance, solution-processed multiscale metallic TCs based on the integration of microscale Ag grid structures and Ag NW networks. These structures provided  $R_s = 1.49 \Omega/\text{sq}$  at  $T_{550 \text{ nm}} = 86\%$ . Highly conductive Ag grids were fabricated by direct imprinting of thermally reduced Ag NPs using the R-mold. The reservoir considerably improved ink filling inside the grid-

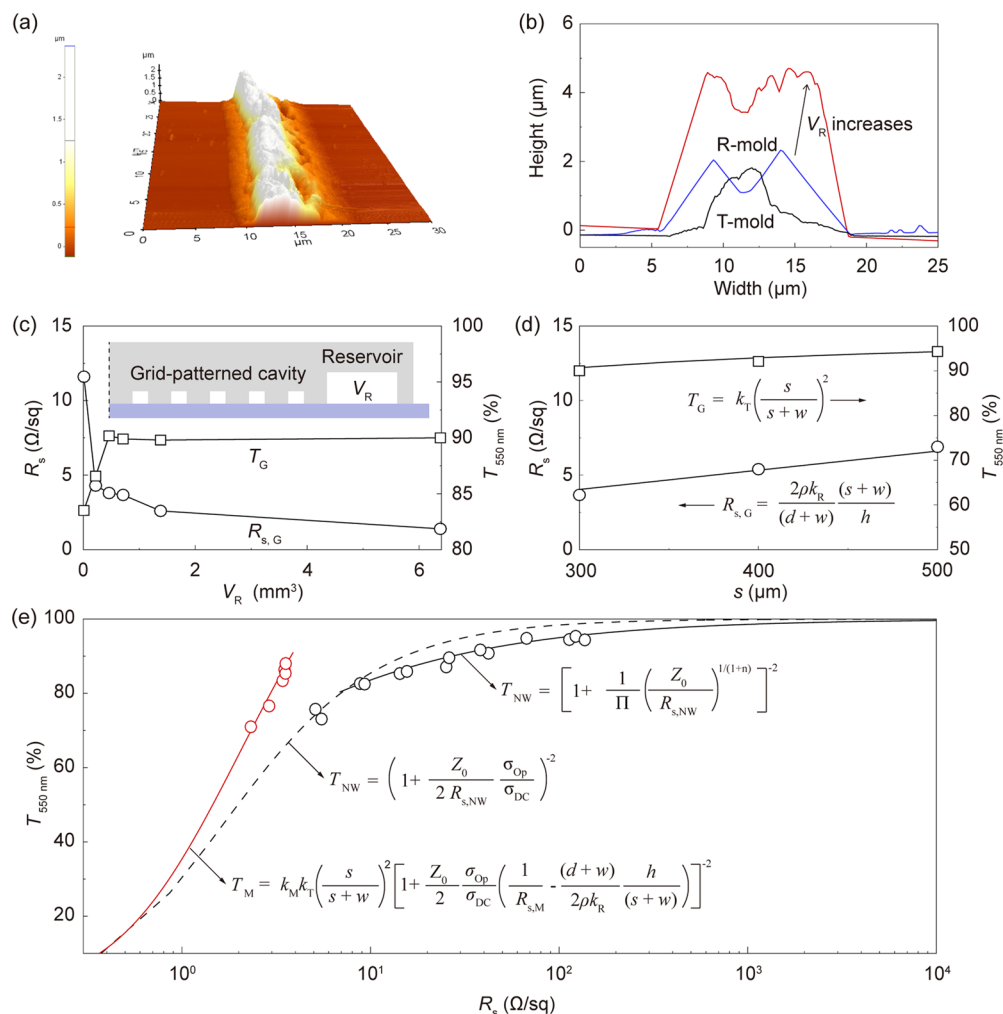


**Figure 2.** (a) AFM image of the Ag grid line. (b) Cross-sectional AFM images of the Ag grid line fabricated using the T-mold or the R-mold ( $V_R = 0.713 \text{ mm}^3$  and  $6.382 \text{ cm}^3$ , respectively). (c) Sheet resistances and transmittances at a wavelength of 550 nm of the Ag grid-based TCs fabricated using the R-mold at different  $V_R$  values. The inset shows a cross-sectional schematic diagram of the R-mold. (d) Sheet resistances and transmittances of the Ag grid-based TCs experimentally measured and theoretically calculated. (e)  $R_s$ - $T$  performances of the multiscale metallic TCs and the Ag NW-only networks.

patterned cavity and reduced the formation of residual layers within the grid spacings. The  $R_s$ - $T$  performances of the Ag NW networks were considerably improved by the incorporation with Ag grids, as measured by experiment and predicted by theoretical modeling. The multiscale metallic structures were successfully embedded into a transparent and flexible UV-curable polymer matrix. The embedded metallic TCs showed reasonable electromechanical and chemical stability, and offered low surface roughness for use in flexible organic solar cells (OSCs).

## 2. RESULTS AND DISCUSSION

**2.1. Fabrication of Multiscale Metallic Transparent Conductors.** A schematic illustration of the process used to fabricate the multiscale metallic TCs based on Ag grid-NWs is shown in Figure 1a. The entire process included two distinct steps: direct imprinting of the thermally reduced Ag NPs and spin-coating of the Ag NWs: (i) Ag ion ink ( $50 \mu\text{L}$ ) with a high metal concentration and no aggregates, was dispensed onto a fluorinated glass substrate. (ii) During the direct imprinting process using the R-mold, the grid-patterned cavity and reservoir were filled with the Ag ion ink at a low pressure

( $<100 \text{ kPa}$ ) and a low temperature ( $60 \text{ }^\circ\text{C}$ ).<sup>42</sup> Note that the ink was supplied to the mold cavity from a liquid film deposited between the mold and the substrate during the direct imprinting using the T-mold. In case of the R-mold, the ink was supplied not only from the liquid thin film, but also by injection from the reservoir as a result of the reservoir's relatively large volume reduction by mechanical deformation of mold. The Ag ions that filled the mold were thermally reduced to form Ag NPs; (iii) after complete solvent evaporation and cooling to room temperature, the R-mold was carefully detached from the substrate. The Ag NP structures were sintered at  $250 \text{ }^\circ\text{C}$  for 5 min. (iv) The Ag NW solution was spin-coated onto the substrate and sintered at  $200 \text{ }^\circ\text{C}$  for 1 min. Figure 1b shows a scanning electron microscopy (SEM) image of the Ag NP structures successfully fabricated over the grid-patterned mold area ( $10.5 \times 10.5 \text{ mm}^2$ ). Negligible residual layers within the grid spacings were observed. The resistivity of the reduced Ag NP structures ( $1.54 \times 10^{-5} \Omega\cdot\text{cm}$ ) was about 10 times higher than that of the bulk Ag ( $1.59 \times 10^{-6} \Omega\cdot\text{cm}$ ). Figure 1c shows a SEM image of randomly oriented Ag NWs coated onto the microscale Ag grid structures. A magnified SEM image revealed that the Ag NW networks overlapped with

the Ag grids with thickness ranging from one to several micrometers.

**2.2. Reservoir Effect.** The grid-patterned cavity should be sufficiently filled with concentrated ink while minimizing the formation of unwanted residual layers. Ink filling of the cavity and the formation of unwanted residual layers within the grid spacings depend on the fluid properties (viscosity and surface tension) and on the mold geometry. Although the fluid properties could be controlled by tuning the solvent properties, the carrier solvent used to prepare the Ag ion ink was difficult to be replaced due to the thermal and chemical instabilities of the Ag ions. The large (or small) cavity volume induced insufficient ink filling (or unwanted residual layers) due to a lack (or an excess) of liquid film between the mold and the substrate. In the T-mold, the grid-patterned cavity had a width ( $w_m$ ) of 15  $\mu\text{m}$ , a height ( $h_m$ ) of 9  $\mu\text{m}$ , and a spacing ( $s_m$ ) of  $\geq 300 \mu\text{m}$ . Figure 2a shows an atomic force microscopy (AFM) image of single Ag grid line, which was smaller than the size of the original mold due to insufficient ink filling, solvent evaporation, and structural shrinkage during the sintering step. The Ag grid-based TCs fabricated using the T-mold did not provide the required performance parameters ( $R_s < 10 \Omega/\text{sq}$  at  $T_{550 \text{ nm}} \approx 90\%$ ). We designed an R-mold with a macroscale cavity with a reservoir length ( $L_R$ ) of  $\geq 250 \mu\text{m}$  and a reservoir height ( $h_R$ ) of 9  $\mu\text{m}$ , which was connected to grid-patterned cavity. In the R-mold, the reservoir volume decreased by greater extent than the microscale cavity volume during mold deformation (e.g., roof collapse), as predicted by finite element method (FEM) simulations of the mold deformation, described further in the Supporting Information (Figure S1). As  $L_R$  increased from 15 to 300  $\mu\text{m}$  at a fixed  $h_R$  of 9  $\mu\text{m}$ , the reservoir volume change ( $\Delta V_R$ ) increased significantly due to the roof collapse. Furthermore, larger  $h_R$  increased the volume change, as predicted by the FEM simulations (Figure S2). The larger  $\Delta V_R$  is, the larger amounts of ink are injected into the grid-patterned cavity. Figure 2b shows cross-sectional AFM images of the Ag grid line fabricated by using the T-mold and the R-molds, respectively. The Ag grid line fabricated by using the T-mold showed the maximum height of 1.9  $\mu\text{m}$ . The maximum height of the Ag grid line fabricated by using the R-mold increased from 2.5 to 4.7  $\mu\text{m}$  due to better ink filling, as  $V_R$  increased from 0.713  $\text{mm}^3$  to 6.382  $\text{mm}^3$ . Figure 2c plots the  $R_s$ - $T$  performances of the Ag grid-based TCs fabricated using the R-mold at different values of  $V_R$ .  $R_s$  for the Ag grid-based TCs fabricated using the T-mold was 11.6  $\Omega/\text{sq}$ , and the corresponding value obtained using the R-mold dramatically reduced to 3.6  $\Omega/\text{sq}$  and to 1.5  $\Omega/\text{sq}$  for  $V_R = 0.713 \text{ mm}^3$  and  $V_R = 6.382 \text{ mm}^3$ , respectively. The resistance fluctuations measured from the metal grids showed below 4.1%, 5.2%, and 11.7%, respectively. The Ag grids fabricated using the R-mold showed higher  $T_{550 \text{ nm}}$  than those obtained using the T-mold;  $T_{550 \text{ nm}}$  for the Ag grids increased from 83.5% to 90% as a result of the thinner residual layers present within the grid spacings due to the larger cavity volume of the R-mold.

**2.3.  $R_s$ - $T$  Performance of the Ag Grid-Based Transparent Conductors.** The sheet resistance ( $R_{s,G}$ ) and optical transmittance ( $T_G$ ) of the Ag grid-based TCs were calculated based on the structural size. The equation used to predict  $R_{s,G}$  was constructed by modifying an expression for obtaining  $R_s$  from a square wire network, suggested by van de Groep et al.<sup>25</sup> The cross-section of the Ag grids was regarded as trapezoidal, and  $R_{s,G}$  was predicted by using the following equations:

$$R_{s,G} = \frac{2\rho k_R (s+w)}{(d+w)h} \quad (1)$$

where  $k_R$  is a correction factor for the sheet resistance,  $\rho$  is the resistivity of the thermally reduced Ag structures,  $h$  is the thickness of the Ag grid line,  $w$  is the bottom width,  $d$  is the top width of the Ag grid line, and  $s$  is the spacing between the Ag grid lines. The value of  $k_R$  depends on a difference between the predicted shape of the grid structures and their actual shape. The correction factor, extracted from experimental results, was determined to be  $k_R = 1.75$ . The mean values of  $h$ ,  $w$ ,  $d$ , and  $s$  for the Ag grid line were 2, 15, 6, and 300  $\mu\text{m}$ , respectively. Also,  $T_G$  is formulated by the following equation:

$$T_G = k_T \left( \frac{s}{s+w} \right)^2 \quad (2)$$

where  $k_T$  is a correction factor for the transmittance. The value of  $k_T$  depended on the unwanted residual layers present within the grid spacings and was extracted from the experimental data. Figure 2d indicates the values of  $R_{s,G}$  and  $T_G$  for the Ag grids fabricated using the R-mold ( $V_R = 0.713 \text{ mm}^3$ ) with different spacings. The experimental results could be suitably fit to the theoretical values, and the correction factor was determined to be  $k_T = 0.99$ .

**2.4.  $R_s$ - $T$  Performances of Multiscale Metallic Transparent Conductors.** When the Ag NW networks were incorporated into the Ag grids using the R-mold ( $V_R = 6.382 \text{ mm}^3$ ), the multiscale metallic TCs showed a superior performance ( $R_s$  of 1.49  $\Omega/\text{sq}$  and  $T$  of 86%). However, the Ag grids fabricated using the R-mold ( $V_R = 0.713 \text{ mm}^3$ ) were used as a reference due to the lower resistance fluctuations. The  $R_s$ - $T$  performances of the Ag NW networks and multiscale metallic TCs are shown in Figure 2e. The effect of the Ag grids on the opto-electrical properties of the Ag NW networks was verified by comparing the performances of the multiscale metallic TCs to those of Ag NW-only networks. In general, the opto-electrical properties of the nanostructured thin films could be described using  $R_s$  and  $T$  as follows:<sup>45</sup>

$$T = \left( 1 + \frac{Z_0 \sigma_{Op}}{2R_s \sigma_{DC}} \right)^{-2} \quad (3)$$

where  $Z_0$  is the impedance of free space (377  $\Omega$ ),  $\sigma_{Op}$  is the optical conductivity, and  $\sigma_{DC}$  is the bulk DC conductivity of the nanostructured thin film. The term  $\sigma_{DC}/\sigma_{Op}$  is often used as a bulk-like FoM, for which larger values generally represent better TC performance. However, experimentally measured values of the Ag NW networks did not agree well with those calculated using eq 3. De et al.<sup>17</sup> suggested that a percolative FoM could account for the discrepancies between the predicted values and experimentally measured values in the very thin film or percolative regime. The opto-electrical properties of the Ag NW networks in the percolative regime ( $T \sim 90\%$ ) were modified from eq 3 as follows:

$$T = \left[ 1 + \frac{1}{\Pi} \left( \frac{Z_0}{R_s} \right)^{1/(n+1)} \right]^{-2} \quad (4)$$

where  $\Pi$  is the percolative FoM, and  $n$  is the percolation exponent. The bulk-like and percolative FoMs of the Ag NW networks were obtained by fitting the experimental results to eqs 3 and 4, respectively. The fitted results gave  $\sigma_{DC}/\sigma_{Op} = 140$ ,

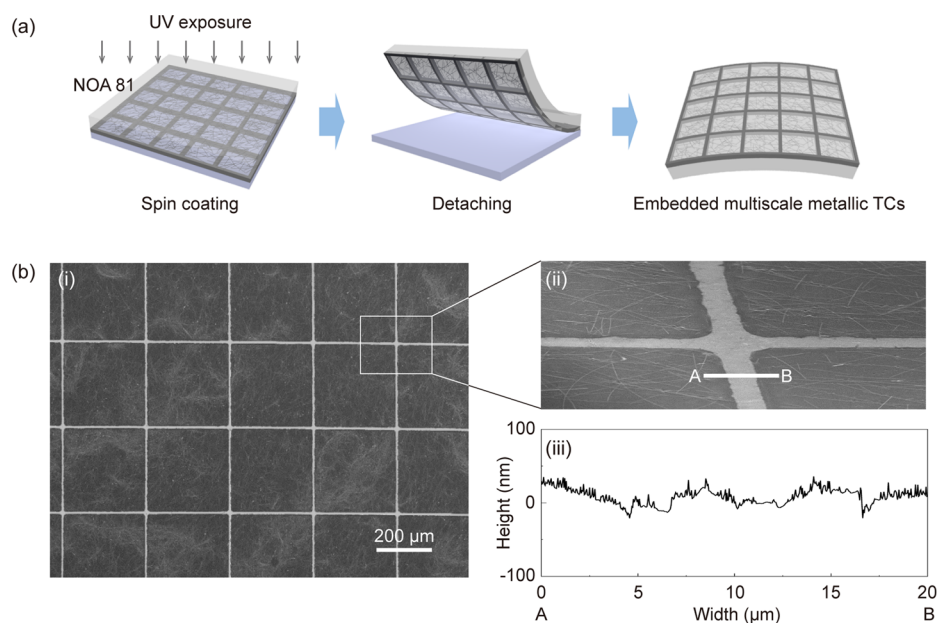


**Figure 3.** (a) Embedding process of the multiscale metallic TC into NOA 81 film. (b-i) SEM images of the multiscale metallic TC-embedded NOA 81 film. (b-ii) Magnified SEM image of the embedded Ag grid-NWs at the intersection. (b-iii) AFM surface profile of the multiscale metallic TC-embedded NOA 81 film.

$\Pi = 70$ , and  $n = 0.8$ . The Ag NW solution prepared with different concentrations was spin-coated onto the Ag grid structures. The multiscale metallic TCs showed lower values of  $R_s$  compared to those obtained from the Ag NW-only networks at a fixed  $T_{550 \text{ nm}}$ . The  $R_s$  values of the Ag NW networks in the percolative regime decreased significantly upon the integration with the Ag grids, even though  $T_{550 \text{ nm}}$  reduced by  $\sim 10\%$ . Assuming that the Ag grids and the Ag NW networks were electrically connected in parallel, the sheet resistance of the multiscale metallic TCs could be expressed simply as  $R_{s,M} = (1/R_{s,G} + 1/R_{s,NW})^{-1}$ , where  $R_{s,G}$  and  $R_{s,NW}$  denote the  $R_s$  values of the Ag grids and the Ag NW networks, respectively. The transmittance of the multiscale metallic TCs was obtained by multiplying the  $T$  values obtained from the Ag grids and the Ag NW networks,  $T_M = T_G \times T_{NW}$ . In the multiscale metallic TCs, the opto-electrical properties of the Ag NW networks could be significantly enhanced in the percolative regime, as the highly conductive Ag grids improved the effective connections of the Ag NW networks.

Equation 4 was not useful for a relatively low transmittance of  $\sim 80\%$ , despite the fact that it was suitably fit to the  $R_s$ - $T$  performances over a transmittance of  $90\%$ . Hence, we used eq 3 to describe the  $R_s$ - $T$  performances in the multiscale metallic TCs over a wide range of transmittance:

$$T_M = k_M k_T \left( \frac{w}{s+w} \right)^2 \left[ 1 + \frac{Z_0 \sigma_{OP}}{2 \sigma_{DC}} \left( \frac{1}{R_{s,M}} - \frac{(d+w)h}{2\rho k_G (s+w)} \right) \right]^{-2} \quad (5)$$

where a correction factor ( $k_M$ ) accounts for a reduction in the transmittance loss due to the overlapping areas of Ag NWs and Ag grids. The experimental results obtained from the multiscale metallic TCs were fitted using  $k_M = 1.03$  in eq 5. Figure 2e reveals that the experimental data obtained from the multiscale metallic TCs were left-shifted relative to the data obtained from the Ag NW-only networks. In other words, for the same optical

transmittance, lower sheet resistance can be achieved by using the multiscale metallic TCs. These results indicated that the opto-electrical properties of the multiscale metallic TCs were considerably enhanced relative to those obtained from the Ag NW-only networks.

**2.5. Flexible, Embedded Multiscale Metallic Transparent Conductors.** After the fabrication of multiscale metallic TCs on the glass substrate, they should be transferred into a polymer substrate for the flexible optoelectronic device applications. By employing a solution-processed and transparent polymer, we can not only achieve a robust embedding/transfer process of multiscale metallic TCs on the polymer substrate, but also reduce a surface roughness that causes the device failure of optoelectronic devices. The embedded metallic TCs based on a polyimide<sup>30,46</sup> or a Norland Optical Adhesive (NOA) film<sup>22,42,44</sup> were provided. A thermally cured polyimide showed excellent mechanical and thermal properties, but did not show a good optical transparency over a wavelength range of  $350$ – $800$  nm. However, a UV-cured NOA film showed an excellent optical transparency over a wide spectral range with a superior mechanical flexibility. The NOA 81 film had a strong adhesion to the metal structures. After a high-temperature sintering process ( $\sim 250$  °C), an effective transfer process of micro/nanoscale metal NP structures was achieved.

Figure 3a shows a schematic illustration of the embedding process, in which the multiscale metallic TCs were transferred and embedded into a polymer substrate (NOA 81 film). The NOA 81 solution was spin-coated onto the substrate and then cured by UV exposure.<sup>44</sup> The multiscale metallic structures on the glass substrate were then transferred to NOA 81 film in water, which intervened between the NOA 81 film and the substrate to reduce the stress formed during detachment.<sup>47</sup> Figure 3b(i) shows a SEM image of the multiscale metallic structures embedded within the NOA 81 film. The Ag grid structures and NW networks were buried below the NOA 81 surface. A magnified SEM image shown in Figure 3b(ii) reveals that the Ag NW networks on the grid spacings were connected

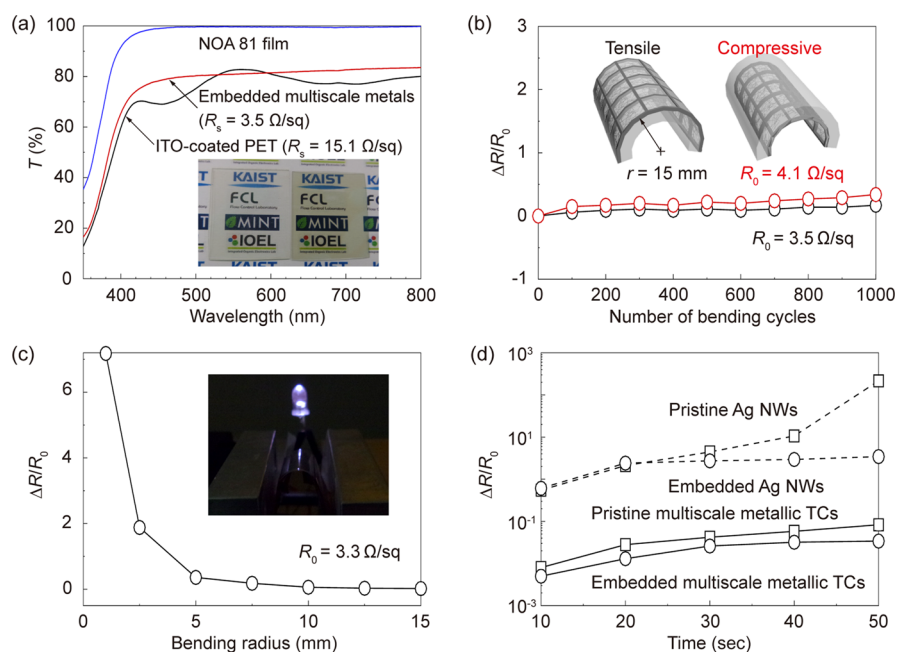


**Figure 4.** (a) Transmittance spectra over a wavelength range of 350–800 nm, of NOA 81 film, the multiscale metal-embedded NOA 81 film, and the ITO-coated PET film. The inset shows photographs of the multiscale metallic TC-embedded NOA 81 film (left) and ITO-coated PET film (right) on the printed paper. (b) Normalized resistance change during the compressive and tensile bending tests. The inset shows schematic images of the tensile and compressive bending tests of the embedded multiscale metallic TCs attached to the PEN sample carrier. (c) Normalized resistance change of the embedded multiscale metallic TCs as a function of the bending radius. (d) Normalized resistance change of the pristine and embedded Ag NWs, and of the pristine and embedded multiscale metallic TCs during the  $\text{O}_2$  plasma exposure (at a power of 20 W).

to the Ag grid structures. The empty spaces in the multiscale metallic network of the Ag grids and NWs were entirely filled with the NOA 81. Figure 3b(iii) shows an AFM surface profile of the embedded multiscale metallic TCs, which presented smooth surfaces with a root-mean-square surface roughness of 10.9 nm and a maximum peak-to-valley value of 56.7 nm.

**2.6. Electromechanical and Chemical Stability.** Figure 4a compares  $T$  and  $R_s$  for the multiscale metallic TC-embedded NOA 81 film with the values obtained from a commercially available ITO-coated polyethylene terephthalate (PET) film. Here, it should be noted that the transmittance spectra for the bare NOA 81 film, the multiscale metallic TC-embedded NOA 81 film, and the ITO-coated PET film represent the values including the substrate. The multiscale metallic TC-embedded NOA 81 film performed better ( $R_s$  of  $3.5 \Omega/\text{sq}$  and  $T_{550 \text{ nm}}$  of 80.9%) than the ITO-coated PET film ( $R_s$  of  $15.1 \Omega/\text{sq}$  and  $T_{550 \text{ nm}}$  of 80.6%). The  $T$  of the ITO-coated PET film fluctuated over the wavelength range 400–800 nm, whereas the corresponding values of the multiscale metallic TC-embedded NOA 81 film remained constant.

Electromechanical stability of TCs is important for the use in flexible optoelectronic devices. Figure 4b plots the normalized resistance change ( $\Delta R/R_0$ ) obtained from the embedded multiscale metallic TCs during compressive or tensile bending tests with a bending radius ( $r$ ) of 15 mm. The inset shows a schematic diagram of the compressive and tensile bending tests. The value of  $\Delta R/R_0$  increased by less than 20% ( $R_0 = 3.5 \Omega/\text{sq}$ ) during the tensile stress test and by less than 32% ( $R_0 = 4.1 \Omega/\text{sq}$ ) during the compressive stress test after 1000 cycles of bending. The small  $\Delta R/R_0$  demonstrated a reasonable electromechanical stability and a good potential for the use in various flexible optoelectronic devices. Figure 4c shows the values of  $\Delta R/R_0$  obtained from the embedded multiscale metallic TCs at different bending radii. The value of  $\Delta R/R_0$

increased by slightly less than a factor of 2, as the embedded multiscale metallic TCs bent up to a 2.5 mm bending radius. The reasonable electromechanical stability was attributed to strong adhesion between NOA 81 film and the multiscale metallic structures, which helped preserve the electrical properties under considerable bending stress. Also, the mechanical adhesion between the embedded multiscale metallic structures and the NOA film was investigated using an adhesive tape peeling test, as shown in Figure S3. The small value of  $\Delta R/R_0$  measured during the tape peeling process indicated reasonable adhesion stability. Figure 4d plots the oxidation stability of the pristine and embedded multiscale metallic TCs and of the pristine and embedded Ag NW networks during  $\text{O}_2$  plasma exposure. The values of  $\Delta R/R_0$  for the pristine and embedded TCs were investigated at different  $\text{O}_2$  plasma exposure times at a power of 20 W. The  $\Delta R/R_0$  values of the pristine Ag NW networks and embedded Ag NW networks increased by more than a factor of 100 and 10, respectively, during the  $\text{O}_2$  plasma exposure for 50 s. The embedded Ag NWs, which were encapsulated by the polymer matrix, were relatively robust against the surface oxidation by the  $\text{O}_2$  plasma. The endurance of the embedded multiscale metallic structures and the pristine multiscale metallic structures was stronger against surface oxidation, which can be attributed to the smaller surface area to volume ratio of the Ag grid structures than the Ag NWs. These results reveal that the embedded multiscale metallic TCs contribute to effectively reduce the performance degradation by metal oxidation during the  $\text{O}_2$  plasma treatment used to improve the solvent wetting for the fabrication of solution-processed flexible optoelectronic devices. Additional chemical stability tests in the presence of solution are described in Figure S4 because the embedded metallic TCs in optoelectronic devices must perform stably during exposure to water, isopropyl alcohol (IPA), or ethanol-based solution.

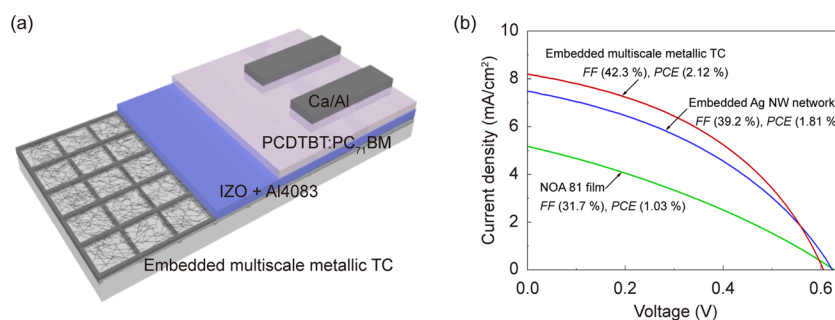


**Figure 5.** (a) Schematic illustration of a flexible OSC based on the embedded multiscale metallic TCs as the anode electrode. (b) Current density–voltage characteristics of the flexible OSCs fabricated using the IZO-coated NOA 81 film, the Ag NW network-embedded NOA 81 film, the multiscale metallic TC-embedded NOA 81 film.

The embedded multiscale metallic TCs showed a reasonable chemical stability during immersion in water, IPA, or ethanol.

**2.7. Application to Flexible Organic Solar Cells.** Figure 5a shows a schematic diagram of flexible OSC prepared with the multiscale metallic TC-embedded NOA 81 film. This device was fabricated to characterize the device performance improvement due to the integration of the Ag grids and Ag NW networks. PEDOT:PSS layers<sup>22,31</sup> or amorphous ITO layers<sup>30</sup> in a normal OSC and ZnO layers<sup>44</sup> in an inverted OSC are generally used to reduce the surface roughness and to collect electrons as a buffer layer. Plasma<sup>22</sup> or UV/Ozone<sup>30</sup> treatment is required for the wettability improvement of solutions on the polymer substrate, while it can induce the performance degradation of metallic TCs to the metal oxidation. In this work, both indium zinc oxide (IZO) layers and PEDOT:PSS layers were coated on the metallic TC-embedded NOA 81 film. Here, the IZO layers protect Ag NWs from the surface oxidation by plasma or UV/Ozone treatment. Figure 5b plots the current density–voltage characteristics of the flexible OSCs using the Ag NW network-embedded NOA 81 film ( $R_s$  of 25.2  $\Omega/\text{sq}$  at  $T_{550\text{ nm}}$  of 87.1%) and the multiscale metallic TC-embedded NOA 81 film ( $R_s$  of 3.5  $\Omega/\text{sq}$  at  $T_{550\text{ nm}}$  of 86%) with the IZO-coated NOA 81 film ( $R_s$  of 200  $\Omega/\text{sq}$  at  $T_{550\text{ nm}}$  of 85%) as a reference. A blend of poly [*N*-9'-hepta-decanyl-2, 7-carbazole-*alt*-5, 5-(40, 70-di-2-thienyl-20, 10, 30-benzothiadiazole)] (PCDTBT) and [6, 6]-phenyl  $C_{71}$ -butyric acid methyl ester (PC<sub>71</sub>BM) was used as a photoactive layer in the device. The OSC based on the IZO-coated NOA 81 film showed a poor performance; a short-circuit current density ( $J_{sc}$ ) of 5.17  $\text{mA cm}^{-2}$ , an open-circuit voltage of ( $V_{oc}$ ) of 0.63 V, a fill factor (FF) of 31.7%, and a power conversion efficiency (PCE) of 1.03%. The OSC based on the multiscale metallic TC-embedded NOA 81 film displayed  $J_{sc}$  of 8.20  $\text{mA cm}^{-2}$ ,  $V_{oc}$  of 0.61 V, and FF of 42.3%, resulting in a PCE of 2.12%. These values exceeded those obtained from the OSC prepared using only the Ag NWs-embedded NOA 81 film with  $J_{sc}$  of 7.48  $\text{mA cm}^{-2}$ ,  $V_{oc}$  of 0.62 V, FF of 39.2%, and PCE of 1.81%. Incorporation of the Ag grid structures into the Ag NW networks increased  $J_{sc}$ , FF, and PCE due to the decrease of  $R_s$ ; however, the OSC based on the multiscale metallic TC-embedded NOA 81 film showed a lower PCE than the OSC based on the ITO-coated glass, which exhibited  $J_{sc}$  of 9.42  $\text{mA cm}^{-2}$ ,  $V_{oc}$  of 0.87 V, FF of 54.7%, and PCE of 4.48%. The lower PCE of the OSC based on the multiscale metallic TC-embedded NOA 81 film may be originated from the low thermal stability of the NOA 81 film during the annealing process in the fabrication of the solution-processed flexible devices. It is speculated that the crumpled NOA 81 surface

could have induced poor interface characteristics, inefficient charge transport, and leakage current, which generally are the origin of low  $J_{sc}$  and  $V_{oc}$ .

### 3. CONCLUSIONS

We demonstrated the fabrication of high-performance, solution-processed, multiscale metallic TCs based on Ag grid-NW networks. The Ag grids with low  $R_s$  and high  $T$  were achieved through the use of a direct imprinting process using a reservoir-assisted mold. This process improved ink filling inside the grid-patterned cavity and reduced the presence of residual layers within the grid spacings, as verified experimentally. The  $R_s$ – $T$  performances of the Ag grid-based TCs were predicted using geometrical calculations. As the Ag grid structures were integrated into Ag NW networks, the performance improvement in the Ag NW networks was demonstrated with fitting the theoretical values to the experimental data. The multiscale metallic TCs were successfully transferred to a transparent polymer substrate, which reduced the surface roughness of the multiscale metallic structures and simultaneously conferred reasonable electromechanical and chemical stability to the device for flexible optoelectronic applications. It is expected that the solution-processed, embedded, and high conductive Ag grids could be used to enhance the opto-electrical properties of other functional materials, such as metal oxides, carbon nanotubes, and graphene, for the use in a variety of next-generation flexible optoelectronic devices.

### 4. EXPERIMENTAL SECTION

**4.1. Materials.** The Ag ion ink (TEC-IJ-060, Inktec), with a 12 wt % metal concentration, consisted of Ag ions (silver alkyl carbamate complexes), a base solvent (methanol and toluene), and additives. The Ag alkyl carbamate complexes are converted to Ag NPs, carbon dioxide, and the corresponding alkyl amines by heating above 60 °C for a few minutes. The ionic bond between the Ag and carbamate anion is considerably weakened by coordination between Ag and an alkyl amine.<sup>48</sup> Ag NWs dispersed in IPA (739448, Sigma-Aldrich) had an average diameter of 115 nm, an average length of 20–50  $\mu\text{m}$ , and a concentration of metal (<0.5%). NOA 81 (Norland Products) is diluted using acetone to improve wetting on the fluorinated glass substrate.

**4.2. Fabrication of PDMS Mold.** The PDMS (Sylgard 184, Dow Corning) was formed by mixing the silicon elastomer kit and a curing agent (10:1), and this mixture was poured onto a SU-8 master. After PDMS curing at 100 °C for 1 h, the PDMS replica of the T-mold (or R-mold) was carefully released from the SU-8 master. A stack of 3 M magic tape on the SU-8 master was used to increase the  $h_R$  of the R-mold. In the T-mold, the grid-patterned cavity was designed with a fixed  $w_m$  of 15  $\mu\text{m}$  and an  $s_m$  of 300–500  $\mu\text{m}$  by calculating the geometrical shadow zone,  $T = s_m^2 / (s_m + w_m)^2$ , required to provide a

transmittance exceeding 90%. At high  $h_m > 15 \mu\text{m}$  (or small  $h_m < 3 \mu\text{m}$ ), a sidewall collapse (or roof collapse) of the mold cavity was present. As these collapses led to the performance degradation of Ag grids, the value of  $h_m$  was limited to  $10 \mu\text{m}$  or less to prevent destruction of the Ag NP structures during the mold detaching process. The R-mold consisted of the grid-patterned cavity and the reservoir with  $L_R \leq 1.5 \text{ mm}$ .

**4.3. Embedding Process.** A glass substrate was treated using 1H,1H,2H,2H-perfluorooctyl-trichlorosilane (448931, Sigma-Aldrich) for 3 min in a vacuum chamber. The Ag grid structures were fabricated using a direct imprinting process involving thermally reduced Ag NPs. The Ag grids were then sintered at  $250 \text{ }^\circ\text{C}$  for 5 min. After the Ag grid structures were patterned on the glass substrate, Ag NW solution was spin-coated onto the substrate and was retreated with fluorinated silane for 2 min in a vacuum chamber. The NOA 81 solution was spin-coated onto the multiscale metallic TCs at 300 rpm for 5 s (thickness =  $300 \mu\text{m}$ ). After UV curing, the multiscale metallic TC-embedded NOA 81 film was carefully released from the glass substrate in air or water.

**4.4. Fabrication of Flexible Organic Solar Cells.** The flexible OSCs were fabricated using the embedded multiscale metallic TCs and the embedded Ag NW networks. IZO layers ( $\sim 100 \text{ nm}$ ) were deposited on the ITO-coated glass, the NOA 81 film, the Ag NW network-embedded NOA 81 film and the multiscale metallic TC-embedded NOA 81 film with the RF sputtering (RF power: 120 W) in vacuum ( $5 \times 10^{-3} \text{ Torr}$ ). After  $\text{O}_2$  plasma treatment (70 W, 1 min), PEDOT:PSS (AI4083,  $\sim 50 \text{ nm}$ ) was spin-coated onto the IZO-coated films. PEDOT:PSS layers were annealed to evaporate residual solvents at  $100 \text{ }^\circ\text{C}$  for 10 min in air. Substrates were moved into a nitrogen-filled glovebox, and then PCDTBT:PC<sub>71</sub>BM (35 mg/mL, 1:4 w/w) in the dichlorobenzene solvent was spin-coated at 1100 rpm for 60 s. PCDTBT:PC<sub>71</sub>BM layers were annealed at  $80 \text{ }^\circ\text{C}$  for 10 min to evaporate the residual solvents. The thickness of the PCDTBT:PC<sub>71</sub>BM layer was measured as 100 nm. Finally, the Ca layer (20 nm) and the Al layer (100 nm) were sequentially deposited on the top of the PCDTBT:PC<sub>71</sub>BM layer through thermal evaporation at  $5 \times 10^{-6} \text{ Torr}$ .

**4.5. Characterization.** The metallic structures were imaged using field-emission SEM (S-4800, Hitachi). Cross-sectional profiles of the pristine and embedded metallic structures were measured using AFM (XE-100, Park Systems). The transmittance of the metallic TCs was measured using a UV-vis-NIR spectrophotometer (V570, Jasco). The sheet resistance of the metallic TCs was measured using two-terminal method<sup>5,14</sup> and four-point probe method (Keithley 4200-SCS). Two electrodes between the metallic TCs, separated by a square area ( $25 \text{ mm}^2$ ), were fabricated using a conductive pen. In particular, CW2200MTP (ITW Chemtronics) was used for the pristine metallic structures, while CW2900 (ITW Chemtronics) was used for the embedded metallic structures.

**4.6. Finite element simulations.** The finite element simulations were carried out using ABAQUS/Explicit. A Neo-Hookean hyperelastic model was used to describe the large deformations of the R-mold with the following parameters:  $C_{10}$  ( $= 0.0401 \text{ MPa}$ ) and  $D_1$  ( $= 0.2500 \text{ MPa}^{-1}$ ). These parameters were obtained from the shear modulus ( $\mu$ ) and bulk modulus ( $\kappa$ ) according to the expressions:  $C_{10} = \mu/2$  and  $D_1 = 2/\kappa$ . A 3D volume mesh for the PDMS mold was generated using 10-node quartic tetrahedral elements, C3D10M.

## ■ ASSOCIATED CONTENT

### Supporting Information

The Supporting Information is available free of charge on the ACS Publications website at DOI: 10.1021/acsami.6b02333.

Figures S1 and S2 show finite element simulations of the reservoir deformation at different reservoir widths and heights, respectively. Figures S3 and S4 show a mechanical adhesion test and an additional chemical stability test of the embedded multiscale metallic TCs, respectively (PDF)

## ■ AUTHOR INFORMATION

### Corresponding Author

\*E-mail: hjsung@kaist.ac.kr (H.J.S.).

### Author Contributions

All authors have contributed to the completion of the manuscript and have given approval to the final version of the manuscript.

### Notes

The authors declare no competing financial interest.

## ■ ACKNOWLEDGMENTS

This work was supported by the Global Leading Technology Program (No. 10042433) funded by the Ministry of Trade, Industry and Energy, and by the Creative Research Initiatives (No. 2016-004749) program of the National Research Foundation of Korea (MSIP).

## ■ REFERENCES

- (1) Song, M.; You, D. S.; Lim, K.; Park, S.; Jung, S.; Kim, C. S.; Kim, D.-H.; Kim, D.-G.; Kim, J.-K.; Park, J.; Kang, Y.-C.; Heo, J.; Jin, S.-H.; Park, J. H.; Kang, J.-W. Highly Efficient and Bendable Organic Solar Cells with Solution-Processed Silver Nanowire Electrodes. *Adv. Funct. Mater.* **2013**, *23*, 4177–4184.
- (2) Kang, M.-G.; Guo, L. J. Nanoimprinted Semitransparent Metal Electrodes and Their Application in Organic Light-Emitting Diodes. *Adv. Mater.* **2007**, *19*, 1391–1396.
- (3) Hong, S.; Yeo, J.; Kim, G.; Kim, D.; Lee, H.; Kwon, J.; Lee, H.; Lee, P.; Ko, S. H. Nonvacuum, Maskless Fabrication of a Flexible Metal Grid Transparent Conductor by Low-Temperature Selective Laser Sintering of Nanoparticle Ink. *ACS Nano* **2013**, *7*, 5024–5031.
- (4) Kumar, A.; Zhou, C. The Race to Replace Tin-Doped Indium Oxide: Which Material Will Win? *ACS Nano* **2010**, *4*, 11–14.
- (5) Vosgueritchian, M.; Lipomi, D. J.; Bao, Z. Highly Conductive and Transparent PEDOT:PSS Films with a Fluorosurfactant for Stretchable and Flexible Transparent Electrodes. *Adv. Funct. Mater.* **2012**, *22*, 421–428.
- (6) Kim, K. S.; Zhao, Y.; Jang, H.; Lee, S. Y.; Kim, J. M.; Kim, K. S.; Ahn, J.-H.; Kim, P.; Choi, J.-Y.; Hong, B. H. Large-Scale Pattern Growth of Graphene Films for Stretchable Transparent Electrodes. *Nature* **2009**, *457*, 706–710.
- (7) Bae, S.; Kim, H.; Lee, Y.; Xu, X.; Park, J.-S.; Zheng, Y.; Balakrishnan, J.; Lei, T.; Kim, H. R.; Song, Y. I.; Kim, Y.-J.; Kim, K. S.; Özyilmaz, B.; Ahn, J.-H.; Hong, B. H.; Iijima, S. Roll-to-Roll Production of 30-Inch Graphene Films for Transparent Electrodes. *Nat. Nanotechnol.* **2010**, *5*, 574–578.
- (8) Zhang, D.; Ryu, K.; Liu, X.; Polikarpov, E.; Ly, J.; Tompson, M. E.; Zhou, C. Transparent, Conductive, and Flexible Carbon Nanotube Films and Their Application in Organic Light-Emitting Diodes. *Nano Lett.* **2006**, *6*, 1880–1886.
- (9) Nasibulin, A. G.; Kaskela, A.; Mustonen, K.; Anisimov, A. S.; Ruiz, V.; Kivisto, S.; Rackauskas, S.; Timmermans, M. Y.; Pudas, M.; Aitchison, B.; Kauppinen, M.; Brown, D. P.; Okhotnikov, O. G.; Kauppinen, E. I. Multifunctional Free-Standing Single-Walled Carbon Nanotube Films. *ACS Nano* **2011**, *5*, 3214–3221.
- (10) Choi, D. Y.; Kang, H. W.; Sung, H. J.; Kim, S. S. Annealing-Free, Flexible Silver Nanowire-Polymer Composite Electrodes Via a Continuous Two-Step Spray-Coating Method. *Nanoscale* **2013**, *5*, 977–983.
- (11) Mutiso, R. M.; Sherratt, M. C.; Rathmell, A. R.; Wiley, B. J.; Winey, K. I. Integrating Simulations and Experiments to Predict Sheet Resistance and Optical Transmittance in Nanowire Films for Transparent Conductors. *ACS Nano* **2013**, *7*, 7654–7663.
- (12) Yu, J.-S.; Kim, I.; Kim, J.-S.; Jo, J.; Larsen-Olsen, T. T.; Sondergaard, R. R.; Hösel, M.; Angmo, D.; Jørgensen, M.; Krebs, F. C. Silver Front Electrode Grids for ITO-Free All Printed Polymer Solar Cells with Embedded and Raised Topographies, Prepared by Thermal

Imprint, Flexographic and Inkjet Roll-to-Roll Processes. *Nanoscale* **2012**, *4*, 6032–6040.

(13) Galagan, Y.; Rubingh, J.-E. J. M.; Andriessen, R.; Fan, C.-C.; Blom, P. W. M.; Veenstra, S. C.; Kroon, J. M. ITO-Free Flexible Organic Solar Cells with Printed Current Collecting Grids. *Sol. Energy Mater. Sol. Cells* **2011**, *95*, 1339–1343.

(14) Hsu, P.-C.; Wang, S.; Wu, H.; Narasimhan, V. K.; Kong, D.; Lee, H. R.; Cui, Y. Performance Enhancement of Metal Nanowire Transparent Conducting Electrodes by Mesoscale Metal Wires. *Nat. Commun.* **2013**, *4*, 2522.

(15) De, S.; Higgins, T. M.; Lyons, P. E.; Doherty, E. M.; Nirmalraj, P. N.; Blau, W. J.; Boland, J. J.; Coleman, J. N. Silver Nanowire Networks as Flexible, Transparent, Conducting Films: Extremely High Dc to Optical Conductivity Ratios. *ACS Nano* **2009**, *3*, 1767–1774.

(16) Bergin, S. M.; Chen, Y.-H.; Rathmell, A. R.; Charbonneau, P.; Li, Z.-Y.; Wiley, B. J. The Effect of Nanowire Length and Diameter on the Properties of Transparent, Conducting Nanowire Films. *Nanoscale* **2012**, *4*, 1996–2004.

(17) De, S.; King, P. J.; Lyons, P. E.; Khan, U.; Coleman, J. N. Size Effects and the Problem with Percolation in Nanostructured Transparent Conductors. *ACS Nano* **2010**, *4*, 7064–7072.

(18) Lee, P.; Lee, J.; Lee, H.; Yeo, J.; Hong, S.; Nam, K. H.; Lee, D.; Lee, S. S.; Ko, S. H. Highly Stretchable and Highly Conductive Metal Electrode by Very Long Metal Nanowire Percolation Network. *Adv. Mater.* **2012**, *24*, 3326–3332.

(19) Lee, J.; Lee, P.; Lee, H.; Lee, D.; Lee, S. S.; Ko, S. H. Ko Very Long Ag Nanowire Synthesis and Its Application in a Highly Transparent, Conductive and Flexible Metal Electrode Touch Panel. *Nanoscale* **2012**, *4*, 6408–6414.

(20) Zhu, R.; Chung, C.-H.; Cha, K. C.; Yang, W.; Zheng, Y. B.; Zhou, H.; Song, T.-B.; Chen, C.-C.; Weiss, P. S.; Li, G.; Yang, Y. Fused Silver Nanowires with Metal Oxide Nanoparticles and Organic Polymers for Highly Transparent Conductors. *ACS Nano* **2011**, *5*, 9877–9882.

(21) Chen, R.; Das, S. R.; Jeong, C.; Khan, M. R.; Janes, D. B.; Alam, M. A. Co-Percolating Graphene-Wrapped Silver Nanowire Network for High Performance, Highly Stable, Transparent Conducting Electrodes. *Adv. Funct. Mater.* **2013**, *23*, 5150–5158.

(22) Choi, D. Y.; Oh, Y. S.; Han, D.; Yoo, S.; Sung, H. J.; Kim, S. S. Highly Conductive, Bendable, Embedded Ag Nanoparticle Wire Arrays Via Convective Self-Assembly: Hybridization into Ag Nanowire Transparent Conductors. *Adv. Funct. Mater.* **2015**, *25*, 3888–3898.

(23) Park, J. H.; Lee, D. Y.; Kim, Y.-H.; Kim, J. K.; Lee, J. H.; Park, J. H.; Lee, T.-W.; Cho, J. H. Flexible and Transparent Metallic Grid Electrodes Prepared by Evaporative Assembly. *ACS Appl. Mater. Interfaces* **2014**, *6*, 12380–12387.

(24) Hu, L.; Wu, H.; Cui, Y. Metal Nanogrids, Nanowires, and Nanofibers for Transparent Electrodes. *MRS Bull.* **2011**, *36*, 760–765.

(25) van de Groep, J.; Spinelli, P.; Polman, A. Transparent Conducting Silver Nanowire Networks. *Nano Lett.* **2012**, *12*, 3138–3144.

(26) Kang, M.-G.; Kim, M.-S.; Kim, J.; Guo, L. J. Organic Solar Cells Using Nanoimprinted Transparent Metal Electrodes. *Adv. Mater.* **2008**, *20*, 4408–4413.

(27) Ghosh, D. S.; Chen, T. L.; Pruneri, V. High Figure-of-Merit Ultrathin Metal Transparent Electrodes Incorporating a Conductive Grid. *Appl. Phys. Lett.* **2010**, *96*, 041109.

(28) Zhang, Z.; Zhang, X.; Xin, Z.; Deng, M.; Wen, Y.; Song, Y. Controlled Inkjetting of a Conductive Pattern of Silver Nanoparticles Based on the Coffee-Ring Effect. *Adv. Mater.* **2013**, *25*, 6714–6718.

(29) Layani, M.; Magdassi, S. Flexible Transparent Conductive Coatings by Combining Self-Assembly with Sintering of Silver Nanoparticles Performed at Room Temperature. *J. Mater. Chem.* **2011**, *21*, 15378–15382.

(30) Jung, S.; Lee, S.; Song, M.; Kim, D.-G.; You, D. S.; Kim, J.-K.; Kim, C. S.; Kim, T.-M.; Kim, K.-H.; Kim, J.-J.; Kang, J.-W. Extremely Flexible Transparent Conducting Electrodes for Organic Devices. *Adv. Energy Mater.* **2014**, *4*, 1300474.

(31) Burgués-Ceballos, I.; Kehagias, N.; Sotomayor-Torres, C. M.; Campoy-Quiles, M.; Lacharmoise, P. D. Embedded Inkjet Printed Silver Grids for Ito-Free Organic Solar Cells with High Fill Factor. *Sol. Energy Mater. Sol. Cells* **2014**, *127*, 50–57.

(32) Santhanam, V.; Andres, R. P. Microcontact Printing of Uniform Nanoparticle Arrays. *Nano Lett.* **2004**, *4*, 41–44.

(33) Kim, E.; Xia, Y.; Whitesides, G. M. Polymer Microstructures Formed by Moulding in Capillaries. *Nature* **1995**, *376*, 581.

(34) Ko, S. H.; Park, I.; Pan, H.; Grigoropoulos, C. P.; Pisano, A. P.; Luscombe, C. K.; Fréchet, J. M. Direct Nanoimprinting of Metal Nanoparticles for Nanoscale Electronics Fabrication. *Nano Lett.* **2007**, *7*, 1869–1877.

(35) Park, I.; Ko, S. H.; Pan, H.; Grigoropoulos, C. P.; Pisano, A. P.; Fréchet, J. M. J.; Lee, E.-S.; Jeong, J.-H. Nanoscale Patterning and Electronics on Flexible Substrate by Direct Nanoimprinting of Metallic Nanoparticles. *Adv. Mater.* **2008**, *20*, 489–496.

(36) Suh, K. Y.; Kim, Y. S.; Lee, H. H. Capillary Force Lithography. *Adv. Mater.* **2001**, *13*, 1386–1389.

(37) Xia, Y.; Whitesides, G. M. Soft Lithography. *Annu. Rev. Mater. Sci.* **1998**, *28*, 153–184.

(38) Wilhelm, E. J.; Jacobson, J. M. Direct Printing of Nanoparticles and Spin-on-Glasses by Offset Liquid Embossing. *Appl. Phys. Lett.* **2004**, *84*, 3507–3509.

(39) Wilhelm, E. J.; Neltner, B. T.; Jacobson, J. M. Nanoparticle-Based Microelectromechanical Systems Fabricated on Plastic. *Appl. Phys. Lett.* **2004**, *85*, 6424–6426.

(40) Park, I.; Cheng, J.; Pisano, A. P.; Lee, E.-S.; Jeong, J.-H. Low Temperature, Low Pressure Nanoimprinting of Chitosan as a Biomaterial for Bionanotechnology Applications. *Appl. Phys. Lett.* **2007**, *90*, 093902.

(41) Oh, Y. S.; Lee, K. H.; Kim, H.; Jeon, D. Y.; Ko, S. H.; Grigoropoulos, C. P.; Sung, H. J. Direct Micro/Nano Patterning of Multiple Colored Quantum Dots by Large Area and Multilayer Imprinting. *J. Phys. Chem. C* **2012**, *116*, 11728–11733.

(42) Oh, Y. S.; Choi, D. Y.; Sung, H. J. Direct Imprinting of Thermally Reduced Silver Nanoparticles Via Deformation-Driven Ink Injection for High-Performance, Flexible Metal Grid Embedded Transparent Conductors. *RSC Adv.* **2015**, *5*, 64661–64668.

(43) Gaynor, W.; Burkhard, G. F.; McGehee, M. D.; Peumans, P. Smooth Nanowire/Polymer Composite Transparent Electrodes. *Adv. Mater.* **2011**, *23*, 2905–2910.

(44) Nam, S.; Song, M.; Kim, D.-H.; Cho, B.; Lee, H. M.; Kwon, J.-D.; Park, S.-G.; Nam, K.-S.; Jeong, Y.; Kwon, S.-H.; Park, Y. C.; Jin, S.-H.; Kang, J.-W.; Jo, S.; Kim, C. S. Ultrasoft, Extremely Deformable and Shape Recoverable Ag Nanowire Embedded Transparent Electrode. *Sci. Rep.* **2014**, *4*, 4788.

(45) Dressel, M.; Grüner, G. *Electrodynamics of Solids: Optical Properties of Electrons in Matter*; Cambridge University Press: Cambridge, 2002.

(46) Ghosh, D. S.; Chen, T. L.; Mkhitarian, V.; Pruneri, V. Ultrathin Transparent Conductive Polyimide Foil Embedding Silver Nanowires. *ACS Appl. Mater. Interfaces* **2014**, *6*, 20943–20948.

(47) Lee, Y.; Bae, S.; Jang, H.; Jang, S.; Zhu, S.-E.; Sim, S. H.; Song, Y. I.; Hong, B. H.; Ahn, J.-H. Wafer-Scale Synthesis and Transfer of Graphene Films. *Nano Lett.* **2010**, *10*, 490–493.

(48) Kwak, W.-G.; Oh, M. H.; Gong, M.-S. Preparation of Silver-Coated Cotton Fabrics Using Silver Carbamate Via Thermal Reduction and Their Properties. *Carbohydr. Polym.* **2015**, *115*, 317–324.

## NOTE ADDED AFTER ASAP PUBLICATION

This paper was published on the Web on April 22, 2016, with minor text errors. The corrected version was reposted on April 25, 2016.